RESEARCH

Open Access

Deep learning for inverse design of low-boom supersonic configurations

Shusheng Chen[1,2]* , Jiyan Qiu[3], Hua Yang[1], Wu Yuan[3]* and Zhenghong Gao[1]

*Correspondence:
sshengchen@nwpu.edu.cn;
yuanwu@sccas.cn

[1] School of Aeronautics, Northwestern Polytechnical University, Xi'an 710072, China
[2] AVIC The First Aircraft Institute, Xi'an 710089, China
[3] Computer Network Information Center, Chinese Academy of Sciences, Beijing 100190, China

Abstract

Mitigating the sonic boom to an acceptable stage is crucial for the next generation of supersonic transports. The primary way to suppress sonic booms is to develop a low sonic boom aerodynamic shape design. This paper proposes an inverse design approach to optimize the near-field signature of an aircraft, making it close to the shaped ideal ground signature after propagation in the atmosphere. By introducing the Deep Neural Network (DNN) model for the first time, a predicted input of Augmented Burgers equation is inversely achieved. By the K-fold cross-validation method, the predicted ground signature closest to the target ground signature is obtained. Then, the corresponding equivalent area distribution is calculated using the classical Whitham's F-function theory from the optimal near-field signature. The inversion method is validated using the classic example of the C608 vehicle provided by the Third Sonic Boom Prediction Workshop (SBPW-3). The results show that the design ground signature is consistent with the target signature. The equivalent area distribution of the design result is smoother than the baseline distribution, and it shrinks significantly in the rear section. Finally, the robustness of this method is verified through the inverse design of sonic boom for the non-physical ground signature target.

Keywords: Low boom configuration, Deep neural network, Augmented Burgers equation, Supersonic transports, Equivalent area

1 Introduction

As a unique acoustic phenomenon during the flight of a supersonic vehicle, a solid sonic boom usually causes a person to be frightened. An enormous overpressure value and a short rise time of the sonic boom may cause permanent damage to the hearing organs, which is also one of the main factors leading to the failure of the supersonic civil aircraft "Concorde" [1]. Therefore, the sonic boom problem is one of the core bottlenecks to be solved in the design of future green supersonic civil aircraft.

Currently, research institutions worldwide have conducted many studies to reduce the intensity of the sonic boom of supersonic civil aircraft. These are mainly divided into the sonic boom suppression technology based on flow control and the aerodynamic layout design method based on different low sonic boom mechanisms. Compared to the sonic boom suppression technology research with a more avant-garde concept, exploring supersonic civil aircraft's low sonic boom shape design is more practical. NASA

confirmed in the SSBD (Shaped Sonic Boom Demonstrator) [2] project that it could effectively change its ground sonic boom signature through the aerodynamic shape of the aircraft, which also provides a solid foundation for the low sonic boom shape design.

Low sonic boom shape design can be divided into two types of positive [3–6] and inverse designs [7–10] from a macro design perspective. The design goal is to improve the sonic boom's ground signature, and the design variable is the vehicle's aerodynamic shape. The positive design refers to the forward search to reduce the far-field sonic boom signal by using an optimal design method to change the aerodynamic shape of the aircraft. The inverse design refers to artificially giving an ideal far-field ground signature. The sonic boom inversion technique directly finds the corresponding aerodynamic shape. Compared with the positive design, the inverse design method is more efficient in carrying out the low sonic boom shape design. For design proposes, Koziel and Pietrenko-Dabrowska et al. [11–18] have carried out many optimization designs by inverse surrogate models and response features. The current research is mainly focused on the sonic boom inverse design [19, 20]. The sonic boom inverse design can be divided into two steps from the design process perspective: target near-field signature matching [21, 22] and target far-field ground signature matching [23, 24]. The target near-field signature matching method specifies the near-field overpressure distribution to infer the corresponding aerodynamic profile in reverse. The target ground signature matching method determines the far-field ground signature distribution to inverse the near-field overpressure distribution. Target near-field signature matching is easier to achieve because fewer factors affect the link between the vehicle's aerodynamic shape and the near-field overpressure distribution. In the process of target far-field ground signature matching, the classical absorption and molecular relaxation effects [25] have a significant influence on the far-field signal, the results obtained by different methods of sonic boom far-field simulation and inverse extrapolation have a considerable difference, and therefore it is the research focus in the sonic boom inverse design. In this paper, the target ground signature matching is studied using the international mainstream high-confidence method for predicting the far-field signals of supersonic aircraft in regular cruises, that is, the far-field signature prediction method based on the Augmented Burgers equation.

In the sonic boom inverse design research, Li et al. [26] proposed a reverse extrapolation method based on the inverse Augmented Burgers equation, that is, by solving the inverse Augmented Burgers equation to reverse the propagation of the sonic boom signal from the ground to the near field. However, the inverse Augmented Burgers equation is inherently pathological, and solving it by introducing regularization will contaminate the real physical solution and bring some other numerical problems. Rallabhandi [27] conducted a study on the inverse equivalent area design of supersonic aircraft. This study uses the discrete concomitant shape optimization method to reduce the sonic boom's intensity. However, the process did not consider the near and far-field signature distribution and was only applicable to the preliminary design of the aircraft. Zhang et al. [19] proposed a sonic boom inverse design method based on Proper Orthogonal Decomposition (POD), which has certain robustness as an efficient inverse design method. But this method has some limitations because POD initially extracts empirical modes for linear superposition, which can only be described approximately for complex

nonlinear systems. Gu et al. [20] used the operator splitting method and the regularized pseudo-parabolic equation to solve the inverse Augmented Burgers equation again, which can invert the equivalent area distribution more accurately. However, this method only reverses the mid-field sound pressure signal to the near field for the signature inversion problem. Ma et al. [28] compared the sonic boom inverse design method based on the POD and discrete concomitant methods. The results showed that the concomitant equation inversion method has better local excitation signal inversion capability. At the same time, the far-field perceived sound pressure level is more accurate.

Machine learning (ML) has demonstrated remarkable power in recent years for numerous applications [29], like image processing, video and speech recognition, genetics, and disease diagnosis. Deep Neural Networks (DNNs), as a vital component of ML, are suitable for solving ill-posed inverse problems. Inverse design problems refer to problems in which the desired output is known, but the inputs must be determined based on this output. In these problems, DNNs have proven to be a powerful tool for learning complex relationships between inputs and outputs, and for generating new designs based on a set of constraints. One of the main advantages of using DNNs in inverse design problems is their ability to capture and model complex, non-linear relationships between inputs and outputs. Unlike traditional approaches, such as rule-based systems or regression models, DNNs can learn these relationships from data and generate new designs based on a set of constraints. This makes them well suited for applications where the relationships between inputs and outputs are not well understood or are too complex to model analytically. Additionally, DNNs have the ability to handle large amounts of data, which is important in many inverse design problems where a large amount of data may be available. This allows them to capture the subtle variations and patterns in the data, leading to more accurate predictions and better designs. In conclusion, the use of DNNs in inverse design problems provides a powerful tool for capturing and modeling complex relationships between inputs and outputs, as well as handling large amounts of data. These advantages make DNNs a valuable tool for solving various inverse design problems in a variety of fields. At present, machine-learning algorithms have some preliminary applications in the aerospace inverse problem. Glaws et al. [30] leveraged emerging invertible neural network tools to enable the rapid inverse design of airfoil shapes for wind turbines. Sekar et al. [31] proposed an approach to perform the inverse design of airfoils using deep convolutional neural networks. Wang et al. [32] developed the framework of nacelle inverse design based on improved Generative Adversarial Networks. Wang et al. [33] proposed an inverse design method for supercritical airfoil based on conditional generative models in deep learning. Ghosh et al. [34] developed a probabilistic framework for inverse aerodynamic design using invertible neural network. However, there is no application of DNNs in sonic boom inverse design. This paper tries to conduct inverse design research based on DNNs to obtain a more accurate near-field sonic boom signature by inversion.

This paper proposes a near-field sonic boom signal inversion method based on the Augmented Burgers equation and DNN, and then details the framework of this inverse design algorithm and sample generation. It verifies the inverse design effect of the method using the standard example of C608 aircraft provided by the 3rd Sonic Boom Prediction Workshop (SBPW-3, 2020). The results show that the method can accurately

invert the far-field ground signature to obtain the near-field overpressure distribution, which provides technical support for optimizing supersonic aircraft's low sonic boom aerodynamic profiles.

2 Mathematical model

2.1 Augmented Burgers equation

The Augmented Burgers equation is a physical model to simulate the propagation of sonic booms in a stratified real atmosphere. A comprehensive introduction about the Augmented Burgers equation is provided by Cleveland [35]. The Augmented Burgers equation includes the effects of nonlinearity, classical dissipation, and molecular relaxation phenomena. The dimensionless Burgers equation is shown in Eq. (1). Where the dimensionless pressure, dimensionless time, and dimensionless sound pipe distance are P, τ, σ. And dimensionless gas dissipation parameters, dimensionless relaxation coefficients, and dimensionless relaxation time are Γ, C_ν, θ_ν. The sound pipe area, sound velocity, and atmospheric density are S, c_0, ρ_0.

$$\frac{\partial P}{\partial \sigma} = P\frac{\partial P}{\partial \tau} + \frac{1}{\Gamma}\frac{\partial^2 P}{\partial \tau^2} + \sum_\nu C_\nu \frac{\partial^2/\partial \tau^2}{1 + \theta_\nu(\partial/\partial_\tau)}P - \frac{(\partial/\partial_\sigma)S}{2S}P + \frac{\partial/\partial_\sigma(\rho_0 c_0)}{2\rho_0 c_0}P. \qquad (1)$$

The five terms on the right-hand side of Eq. (1) are the nonlinear effect term, the classical dissipation effect term, the molecular relaxation effect term, the geometric diffusion effect term, and the atmospheric stratification effect term, which represent the effects of the corresponding physical impact on the sound pressure signal, respectively.

2.2 Deep neural network

Deep learning is a specialized branch of machine learning that employs artificial neural networks with multiple hidden layers to tackle complex issues, including image and speech recognition. One widely utilized neural network architecture in deep learning is the Multilayer Perceptron (MLP) network. The MLP network presents several advantages, including its capacity to model nonlinear relationships, process extensive datasets, and produce predictions based on the analyzed data. Furthermore, MLP networks possess the capability to continuously learn and improve through training, rendering them ideal for purposes such as predictive modeling and pattern identification.

MLP is one of the simplest and most effective DNN, consisting of an input layer, hidden layers (intermediate layer), and an output layer. Each layer contains several neurons, as shown in Fig. 1, where each neuron has a different bias and the same activation function. As the base module of the multilayer perceptron, the neuron takes the vector as the input, calculates the weighted sum of the inputs, then adds bias, and finally inputs the activation function to get the generated scalar output. Where x_0 to x_n are the values of the neurons in the previous layer, w_i is the weight corresponding to each neuron, b is the bias, and f is the activation function.

Any two nodes between adjacent layers correspond to a weight. All nodes of the previous layer are used as inputs to the subsequent layer. A node in the hidden layers
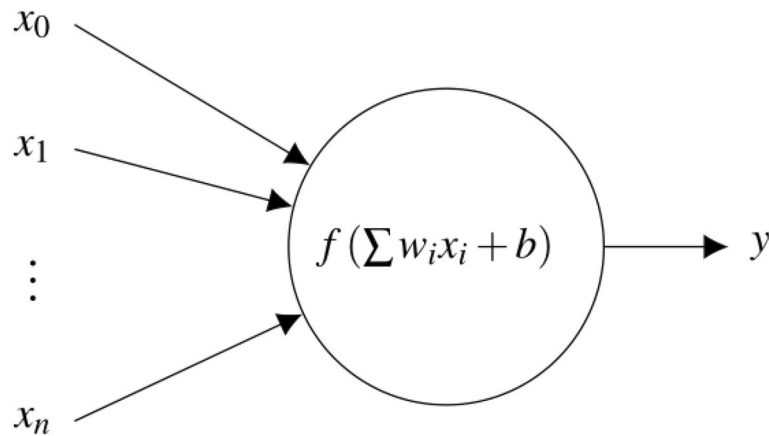
Fig. 1 Neurons schematic diagram

and output layer is connected to all nodes of the last layer, and the result is generated by applying an activation function to the values obtained from these nodes. Sum up the value of each incoming connection multiplied by the weights plus the overall bias, and then apply the activation function. As weights and biases of the whole network, the weight and bias parameters must be adjusted through the training process. The structure of the MLP network used in this paper is shown in Fig. 2, which contains one input layer, one output layer, and six hidden layers for a total of eight layers. Each layer has 400 neurons. Several neurons are omitted in this figure. Because the sonic boom data value domain involves negative numbers, the tanh function is used as the activation function, and the network is trained using the Adam optimizer. During training, both input and output data are normalized so that both input and output are one-dimensional vectors with 400 real numbers. The Adam optimization algorithm has been selected for training the deep neural network (DNN),
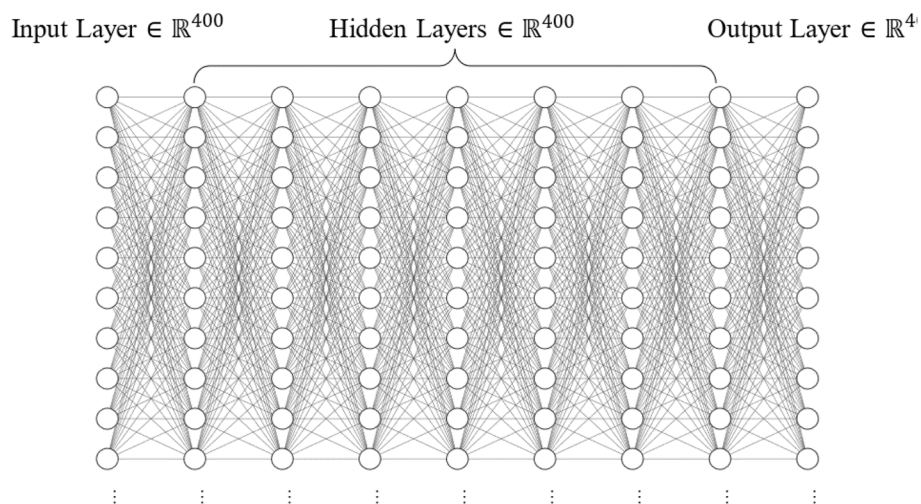
Fig. 2 MLP network structure

with the learning rate γ fixed at 5×10^{-4}. Additionally, the β_1 parameter has been set to 0.9, the β_2 parameter to 0.999, and the θ_0 parameter to 1×10^{-8}.

3 MLP inverse design framework and sample generation

3.1 Inverse design algorithm framework

This article proposes a high-efficiency method based on MLP to find the shape of the aircraft corresponding to a given far-field ground signature. Given the far-field signature, the near-field signature corresponding to the target far-field signature is obtained through the MLP, and then the shape of the aircraft (here refers to the area distribution) corresponding to the near-field signature is obtained by the Abel inverse transform. Figure 3 shows the flow diagram of the inverse design.

Figure 4 shows the entire inverse design framework process, where each process step is shown below.

1) Initialization: Define the baseline near-field overvoltage distribution as the initial optimization value; generate the ideal ground signature as the optimization target.
2) Add perturbation: Add perturbation to the baseline near-field using triangular and sawtooth waves to generate several perturbed near-field curves.
3) Calculation of far-field: The far-field signatures corresponding to the near-field overvoltage distribution after each perturbation is calculated using the Augmented Burgers equation method.
4) Train DNN: Several obtained data are used as the training samples of the DNN. Specifically, the acquired far-field baseline signature is subtracted from the far-field signature corresponding to the baseline near-field signature to obtain the input samples of the DNN; the perturbed near-field signature is removed from the baseline near-field signature to get the output sample data; finally, the Adam optimization algorithm is used to train the DNN.
5) Deep learning inversion: After completing the network training, the difference between the optimized target far-field signature and the far-field signature calculated from the baseline near-field is fed into the DNN to obtain a difference between the inversion result and the baseline near-field, and the inverse near-field result is obtained by adding this result with the baseline near-field.
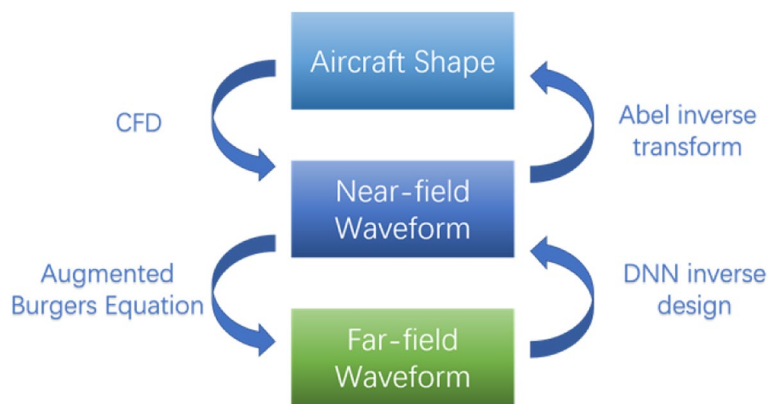

Fig. 3 The flow diagram of the inverse design
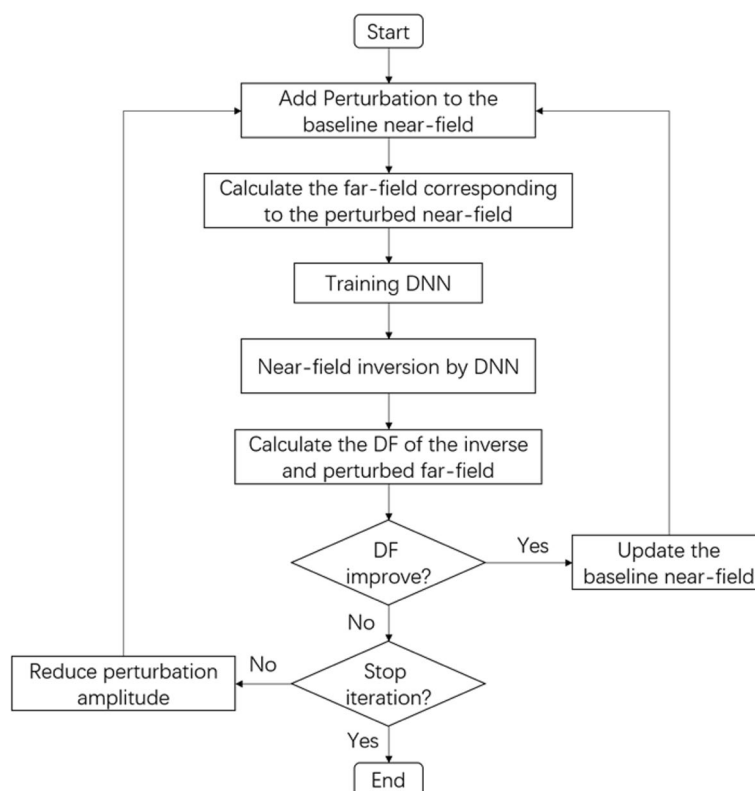
Fig. 4 The inverse design framework process

6) Calculation of inversion DF (Distance Function): The far-field signatures corresponding to the near-field results are obtained by the Augmented Burgers equation. Here, DF is a measure suitable for expressing similarity.

7) Determine DF improvement: If the distance between this inverse design far-field signature and the target far-field signature is improved compared to the previous iteration, then update or replace the baseline near-field signature by this inverse design result, and jump to step 2, otherwise enter step 8.

8) Reduce perturbation amplitude: The setting amplitude attenuation rate is 0.9, and the length attenuation rate is 0.9, reducing the amplitude and length of the perturbation, narrowing the sampling range, and jumping to step 2. When the perturbation amplitude drops to the set range, the whole process is stopped.

3.2 Generation of perturbation data

The triangular and sawtooth waves are used to disturb the near-field over-pressure distribution. The three waveforms are symmetric triangular waves, a right sawtooth wave, and a left sawtooth wave, as shown in Fig. 5.

Three waves of different amplitudes and lengths are added to the baseline near-field over-pressure distribution to form the perturbation, and different amplitudes and lengths are shown in Fig. 6.
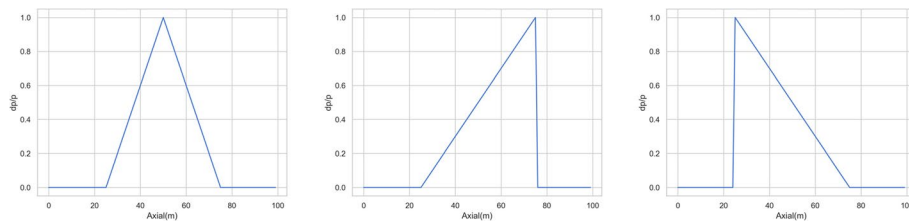
Fig. 5 A diagram of the triangular wave, right sawtooth wave, and left sawtooth wave
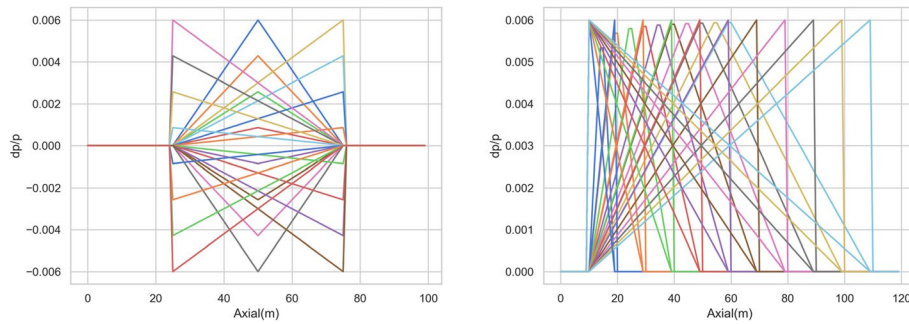
Fig. 6 Amplitude and length perturbations of different waves

Fig. 7 C608 aircraft

4 Validation and optimization

### 4.1 Program verification of sonic boom forwarding propagation equation

In this paper, the study is carried out using the standard example of the C608 aircraft provided by the AIAA Third Sonic Boom Prediction Workshop (SBPW-3, 2020) [36], as shown in Fig. 7, with the inflow Mach being 1.4, the angle of attack being 0°, and the flight altitude being 16,215.36 m. The sonic boom near-field input signal is calculated using the in-house CFD solver [37, 38], and the far-field ground signature is computed by a self-developed sonic boom program [19, 20, 39]. The SST (Shear-Stress-Transport)

turbulence model [40] is adopted for CFD numerical simulation, and the near-field distance is three times the length of the C608 aircraft ($z = 82.29\,\mathrm{m}$). The unstructured hybrid grid provided by SBPW-3 is used [36]. The number of nodes of this half-mode grid is about 502.1 million. The spatial grid density $NZ = 20{,}000$ and the temporal grid density $NT = 50{,}000$ were chosen for the study when calculating the far-field ground signature using the Augmented Burgers equation.

Figures 8 and 9 compare the differences between the currently calculated near-field and far-field signatures and the published data of SBPW-3 [36], respectively, where the red and black lines are the SBPW-3 data, and the solid green line is the data calculated by the self-developed program. It can be found that the predicted near-field and far-field signatures overlap with the SBPW-3 data and achieve a reasonable precision, indicating that the accuracy of the calculation of the self-developed CFD program and the sonic boom program meets the requirements. The near-field overpressure distribution varies at a high frequency, with multiple peaks and valleys. Due to the classical absorption, molecular relaxation effect, etc., the atmosphere has a low-pass filter-like nature and sonic energy, and high-frequency pulsations in the atmospheric propagation process are consumed as internal energy. Thus, the far-field ground waveform is smoother.

4.2 Inverse design example configuration

The C608 vehicle near-field is used as the baseline near-field, and the target far-field is inverted using DNN. Based on Plotkin's proposal for shaping the low sonic boom signature [41], the original ground signature was modified to a sine wave-like shape as the target signature (thereby suppressing the energy in the high-frequency portion of the sonic waves). The original baseline and target ground signature are given in Fig. 10. The
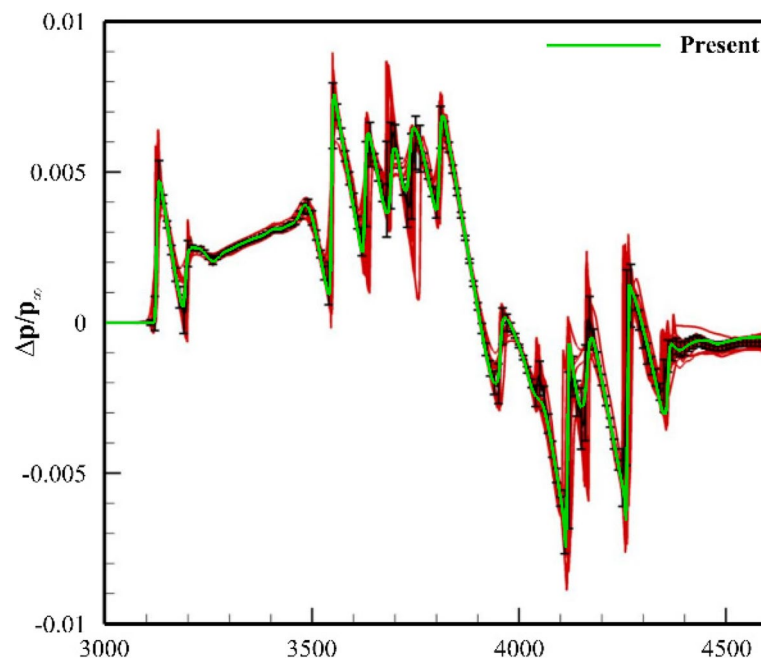
Fig. 8 Comparison between near-field overvoltage value distribution and SBPW-3 data
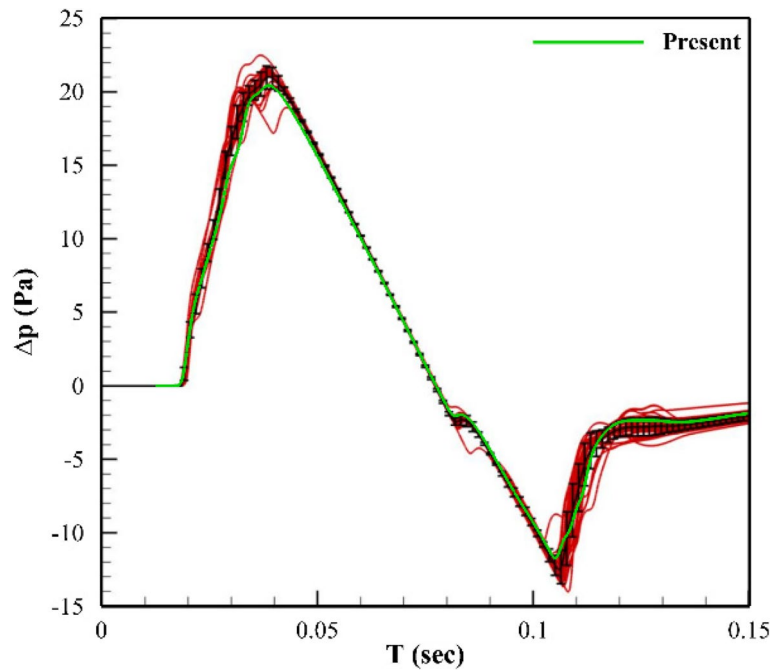
Fig. 9 Comparison between far-field ground signature and SBPW-3 data
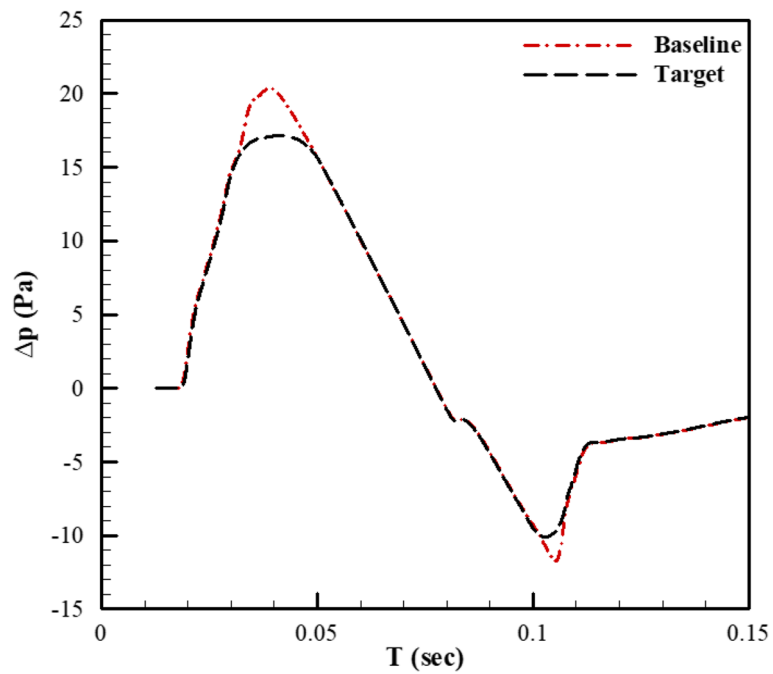
Fig. 10 Target far-field signature

perceived noise level (PLdB) represents the ground sonic boom intensity, and the perceived noise level of the shaped waveform is reduced by 1.5061 PLdB.

The L2 norm is used to describe the closeness of the design result and the target waveform, i.e., the objective function of optimization is the similarity between the disturbed far-field and the target far-field, which is calculated as

$$DF = \frac{\sqrt{\sum_{i=1}^{S} \left(P_{dist}^{i} - P_{tar}^{i}\right)^2}}{S}, \tag{2}$$

where DF is the similarity to be calculated, P_{dist}^{i} is the i-th point of the disturbed far-field vector, P_{tar}^{i} is the i-th point of the target far-field vector, and S is the number of points of the discrete ground signature. The smaller the DF, the higher the similarity.

The baseline near-field overpressure distribution is perturbed to generate 2400 samples of near-field data, as shown in Fig. 11. The blue line is the unperturbed near-field curve, and the perturbed range only contains the part of the aircraft that needs to be reshaped. Considering the magnitude and period of the flow field itself, the maximum magnitude is 0.006 in absolute value, and the maximum length is 100. In this paper, the training of DNN is carried out on a domestic supercomputing platform ("Dongsheng-1"), which uses a heterogeneous hardware environment to run the program and can significantly reduce the algorithm's running time.

4.3 Cross-validation and optimization results

The importance of obtaining high-quality and reliable results cannot be overstated. To that end, K-fold cross-validation is employed as a technique to assess the performance of the machine learning model under investigation. This step is deemed essential in the validation process of the results obtained from the model. The objective of the K-fold cross-validation is to confirm the generalizability of the results obtained from the proposed model, rather than being solely specific to the training data. In K-fold cross-validation, the value of k increases from 3 to 30. Specifically, 2400 samples are randomly divided into k equal parts. The i-th of them is selected as the
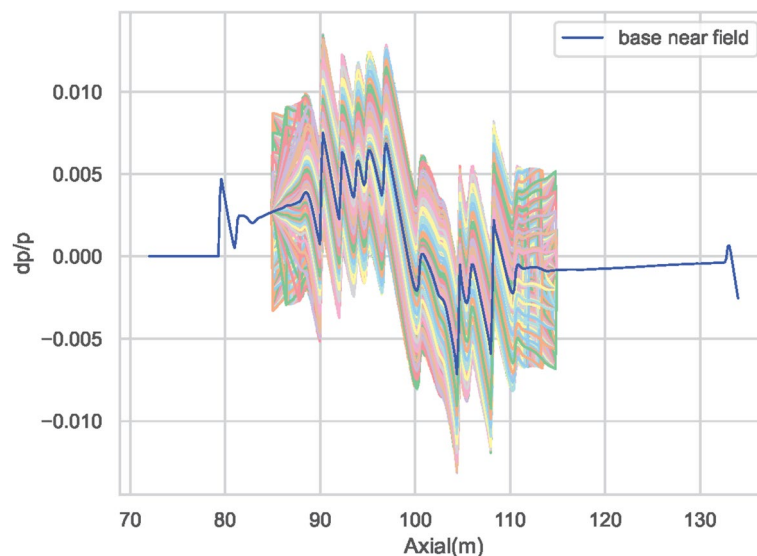
Fig. 11 Near-field data samples

validation set, totaling 2400/*k* samples. The remaining part is the training set, totaling $2400 \times (k\text{-}1)/k$ samples. The structure of the training network is kept constant. Finally, the network models trained with different *k* and *i* are evaluated. The evaluation method uses this network model to inverse the target far-field signature and then forward the near-field signature obtained from the inversion to obtain the design far-field signature corresponding to the inversion result, called $P_{k, i}$. Calculate the similarity *DF* between P_t and $P_{k, i}$. The results are shown in Table 1. The maximum *DF* value, minimum *DF* value, and average *DF* value for different *i* at each value of *k* are shown here. In Table 1, the three numbers marked in red indicate the network models corresponding to the smallest min *DF*, max *DF*, and Avg *DF*, respectively. The networks are trained when $k = 20, 11, 16$.

The results of plotting all the above data into a heat map are shown in Fig. 12. Where the horizontal coordinates are the *k* values and the vertical coordinates are the *i* values. Since *i* is always less than *k*, this graph only has importance in the lower-left region, and the value in the chart is *DF*.

According to cross-verification, the value of the box line can be drawn in different *k* conditions, as shown in Fig. 13. These include the upper limit, lower limit, median, and two quartiles of the cross-validation result *DF*. Connect the two quartiles to draw the box, and then connect the upper and lower limits with the box. The median is in the middle of the box, and the dot represents the abnormal value. The abnormal value is usually eliminated in the process of data analysis.

Finally, the deep neural network trained at $k = 16$ is selected as the final model.
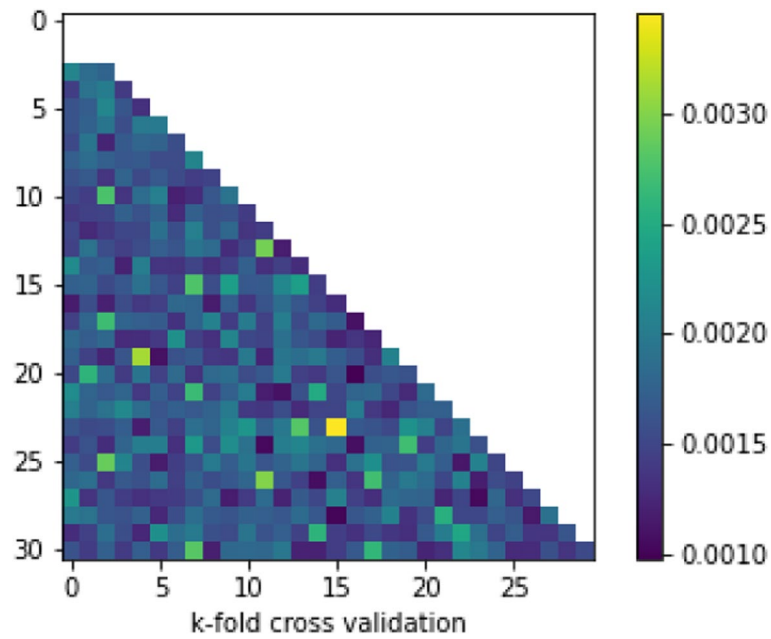
Figure 14 shows the iterative convergence process of the optimized objective function, showing that the objective function does not decrease after the 12th iteration. Figure 15 shows the mean squared error of the training set and validation set of the 6th iteration of the DNN.

Figure 16 gives the corresponding ground signature with the lowest perceived noise level among all optimization results, from which it can be seen that the optimized ground signature achieves a significant shaping effect. The initially sharp compressional waveform is optimized to a relatively flat waveform with minor fluctuations.
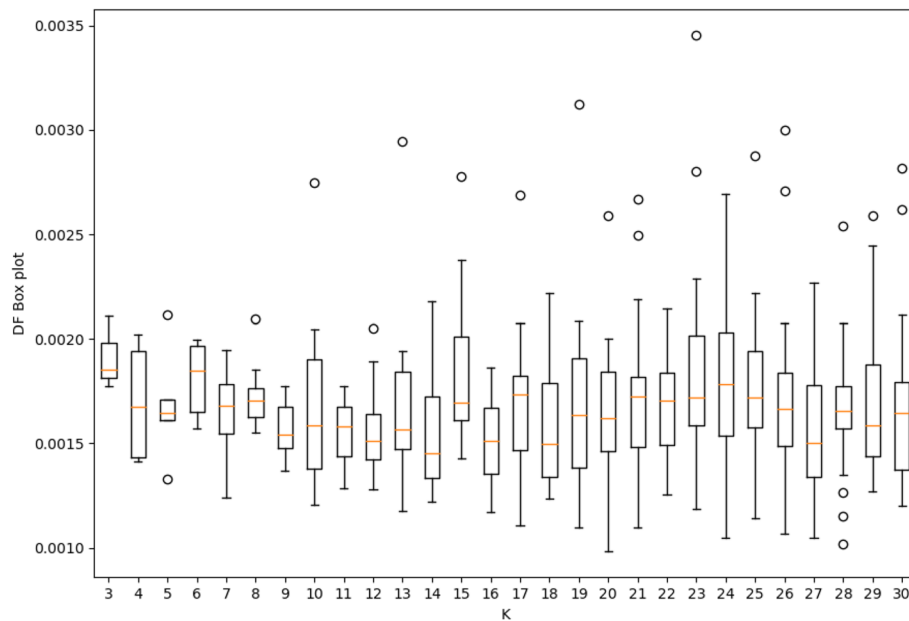
Table 1 Cross-validation results

| *k*	Min *DF*	Max *DF*	Avg *DF*	*k*	Min *DF*	Max *DF*	Avg *DF*
3	0.001775	0.002109	0.00191233	17	0.001105	0.002687	0.00173324
4	0.001412	0.00202	0.00169625	18	0.001237	0.00222	0.00157633
5	0.001329	0.002114	0.0016824	19	0.001096	0.003124	0.00168726
6	0.001573	0.001997	0.00181083	20	**0.000982**	0.002588	0.00165945
7	0.001241	0.001946	0.00164714	21	0.001098	0.002668	0.00171462
8	0.001554	0.002095	0.001732	22	0.001254	0.002143	0.00167918
9	0.001367	0.001776	0.00156622	23	0.001188	0.003455	0.00186491
10	0.001205	0.00275	0.0017061	24	0.001049	0.002694	0.0017695
11	0.001287	**0.001773**	0.00155546	25	0.001142	0.002878	0.00175728
12	0.00128	0.002049	0.00157542	26	0.00107	0.002998	0.00172508
13	0.001176	0.002943	0.00169585	27	0.001046	0.00227	0.0015487
14	0.001223	0.002179	0.00154943	28	0.00102	0.002538	0.00167604
15	0.001427	0.002776	0.00184773	29	0.001269	0.002591	0.00167917
16	0.00117	0.001863	**0.00150944**	30	0.001201	0.002817	0.001653

**Fig. 12** Heat map of cross-validation results

The near-field signature corresponding to the optimal ground signature is given in Fig. 17. It can be seen that the initially flat waveform is optimized to a repeated oscillation waveform. These sharp compressional and expansion waves are suppressed by the classical atmospheric dissipation and molecular churning effects during the propagation process and eventually become relatively flat as they approach the ground.

Fig. 13 Box diagram of cross-validation results
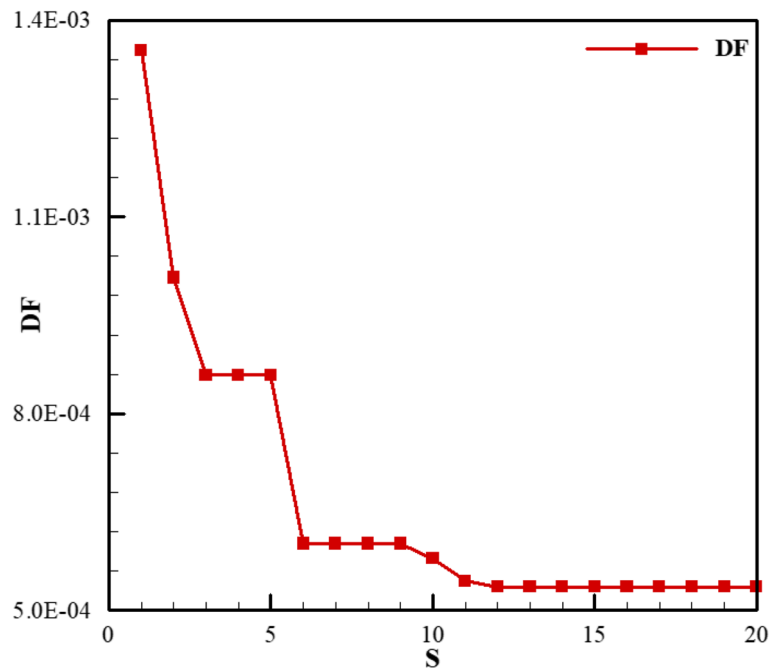
Fig. 14 Convergence process of the optimized objective function
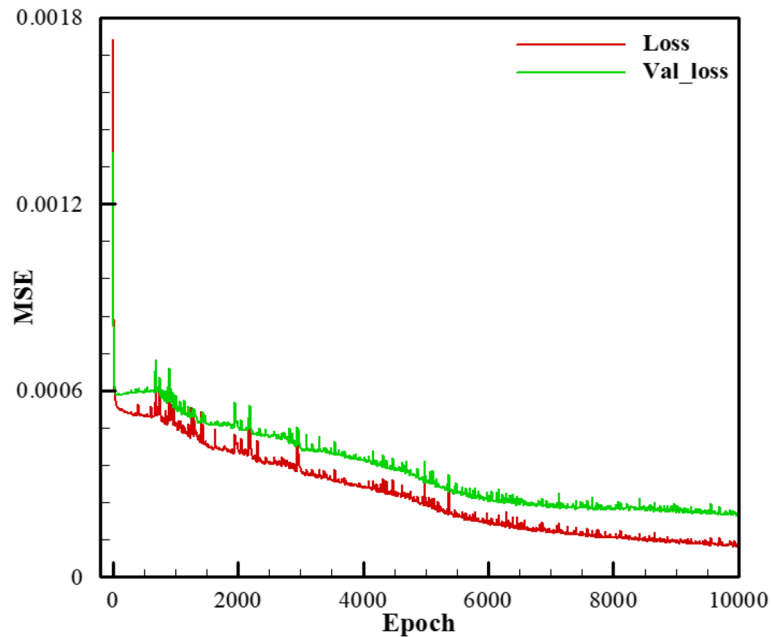

Fig. 15 Mean squared error of training set and validation set

Improvement of optimization is achieved via shaping the original near-field signature into wiggles and damping it by atmospheric attenuation.
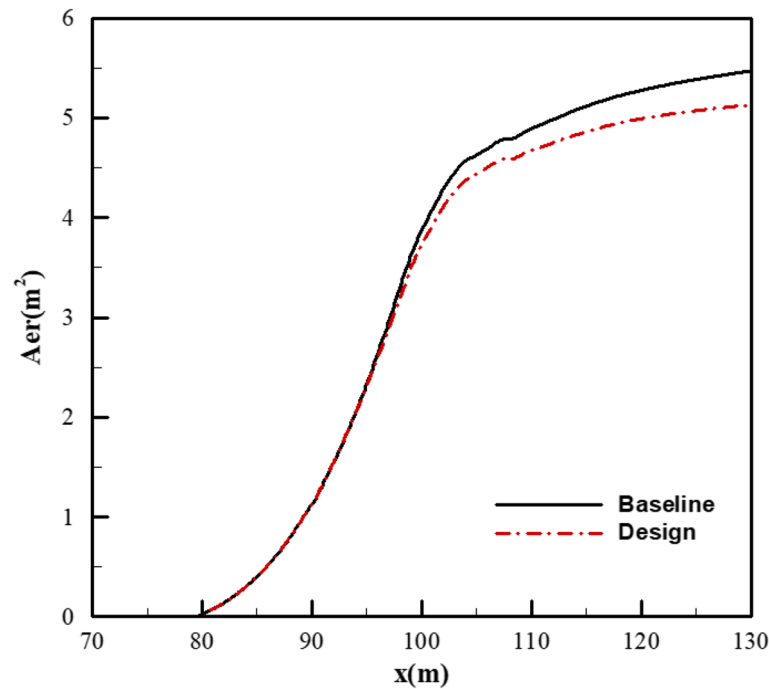
Once the near-field overpressure distribution is determined, the equivalent area distribution for the final design can be obtained by the Abel inverse transform [26] as follows.
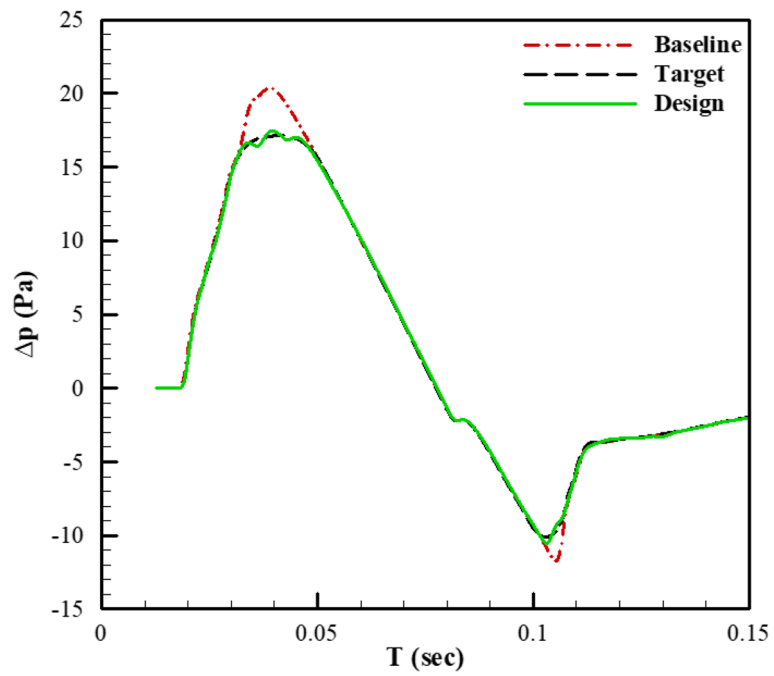
Fig. 16 Comparison of optimized ground signature and target signature
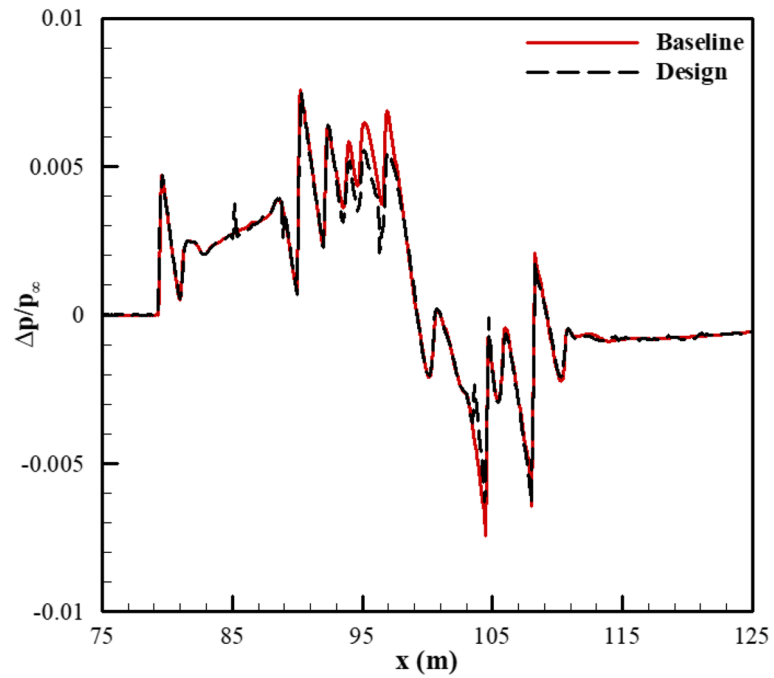
Fig. 17 Comparison of optimized near-field signature and baseline signature

Fig. 18 Comparison of equivalent area distributions

$$A_e(x) = \frac{\sqrt{2R \times \sqrt{M^2-1}}}{\gamma M^2} \int_0^x \left(\frac{dp}{p}\right)\sqrt{x-y}dy. \tag{3}$$

Note that the supersonic profile must satisfy the slender body assumption [42] to use the above equation.

Based on Eq. (3), the equivalent area distributions of the design and initial shapes can be obtained using numerical integration, and a comparison of the equivalent area distributions is presented in Fig. 18. Here, the equivalent area distribution considers the vehicle's volume and lift contributions.

As seen in the latter part of Fig. 18, there is a very significant shrinkage at the tail end of the optimized shape, which represents a loss of volume in this part of the airframe (assuming that the lift distribution remains constant before and after the optimization). In addition, the area distribution of the design shape is smoother compared to the equivalent area distribution of the initial shape.

4.4 Discussions on the DNN inverse design method

In this section, the robustness of the present method is examined when non-physical solutions are set as the target ground signature. The peak and valley of the far-field ground signature are horizontal straight lines. This ground signature is physically non-existent because there is no horizontal straight line in the actual ground waveform. The DNN models and other parameters are the same as the optimization example in Section 4.2 except for the target ground signature. Figure 19 gives the optimized ground signature against the baseline and target. Figure 20 provides the optimized near-field signature against the baseline. As shown in Figs. 19 and 20, the optimized ground signature matches the target to a
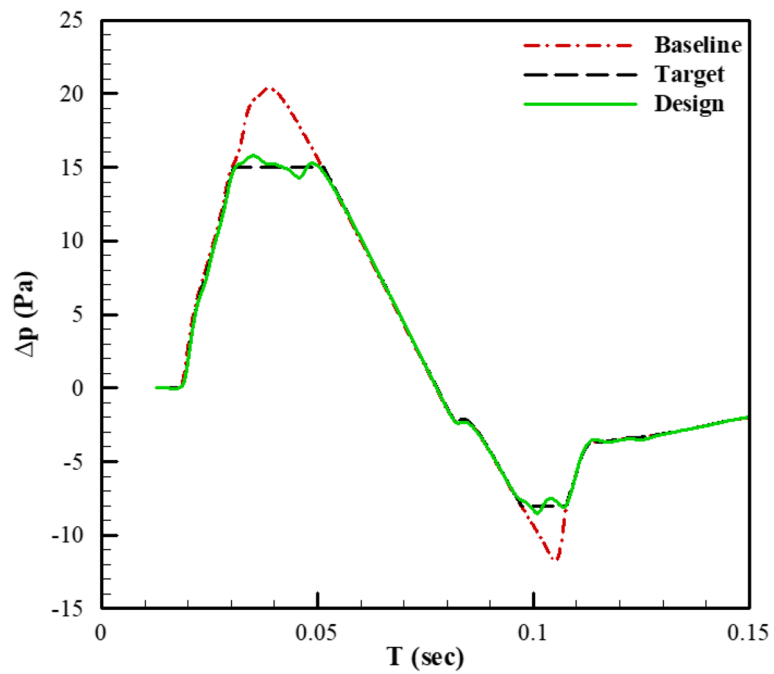
Fig. 19 Optimized ground signature matching a physically non-existent target
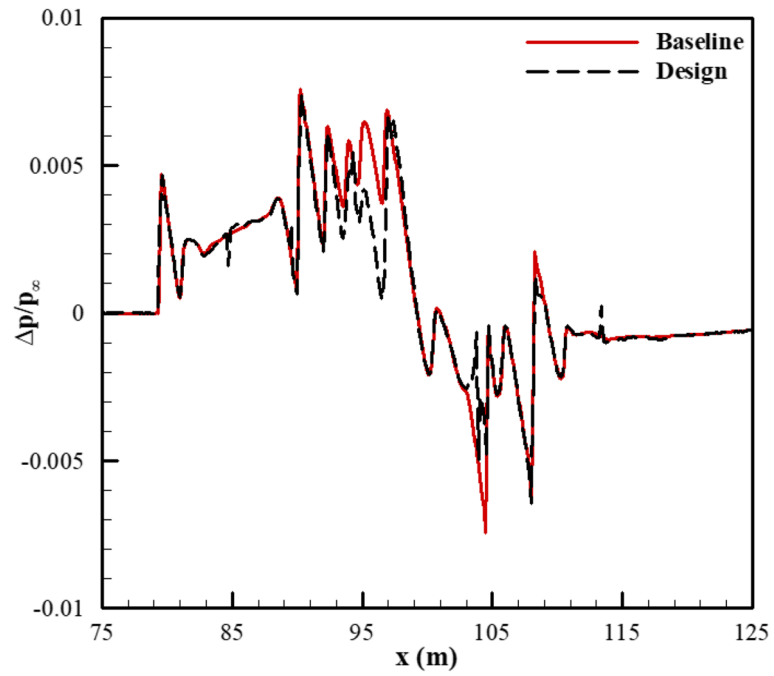
Fig. 20 Optimized near-field signature matching a physically non-existent target

great extent, although the target ground signature is non-physical. The optimized near-field and baseline signatures are reversed at multiple peaks and troughs.

5 Conclusions

This paper proposes a deep neural network-based inversion method for near-field sonic boom signals of supersonic aircraft, aiming to shape the ground signature into the desired target. And its feasibility in low sonic boom inverse design optimization is verified by the C608 vehicle example. The method can be applied to the optimized design of future supersonic aircraft's low sonic boom aerodynamic shape. Some conclusions can be drawn as follows.

1) The forward propagation program of sonic boom based on the Augmented Burgers equation can accurately simulate various physical processes of the sonic boom signal propagation in the natural atmosphere. It can effectively improve the simulation accuracy of the rise time to meet the needs of engineering applications.
2) A deep neural network-based sonic boom inversion method is used to inverse the target far-field ground signature to obtain the near-field overpressure distribution, which is a repeatedly oscillating waveform compared to the original flat baseline near-field waveform but has little effect on the far-field signature.
3) Using the sonic boom forward propagation program to calculate the inversion of the near-field overpressure distribution, the final ground far-field waveform and the target waveform match and achieve a noticeable shape modification effect.
4) The equivalent area distribution of the final design is smoother than the initial shape. It shrinks significantly in the rear section, which provides technical support for subsequent design optimization based on the equivalent area distribution.
5) A non-physical ground signature is set as the target to test the robustness of this inverse design method, and it is shown that this method is robust enough for various inputs. This nature is designer-friendly and does not require extensive sonic boom engineering experience for aircraft designers.

In future endeavors, more sophisticated and appropriate neural networks will be employed to extract the inherent features of the data, with the aim of elevating the accuracy of the network. Furthermore, to enhance the efficiency of the program, optimization of the inversion algorithm will be pursued, in an effort to attain an optimal equilibrium between precision and speed. In addition, the target signature is relevant for inverse design methods, because it is often unclear whether the assumed target characteristics do correspond to the optimum designs in a forward sense. Thus, the target characteristics of sonic booms deserve further research for complex supersonic aircraft.

Availability of data and materials
The datasets generated during the current study are available from the corresponding author upon reasonable request.

Declarations

Competing interests
The authors declare that they have no known competing financial interests or personal relationships that could have appeared to influence the work reported in this paper.

References

1. Zhang LW, Song WP, Han ZH, Qian ZS, Song BF (2022) Recent progress of sonic boom generation, propagation, and mitigation mechanism. Acta Aeronaut Astronaut Sin 43(12):25649 (in Chinese)
2. Pawlowski JW, Graham DH, Boccadoro CH, Coen PG, Maglieri DJ (2005) Origins and overview of the shaped sonic boom demonstration program. Paper presented at the 43rd AIAA aerospace sciences meeting and exhibit, Reno, 10–13 January 2005
3. Song WB, Keane AJ (2007) Surrogate-based aerodynamic shape optimization of a civil aircraft engine nacelle. AIAA J 45(10):2565–2574
4. Koziel S, Leifsson L (2013) Surrogate-based aerodynamic shape optimization by variable-resolution models. AIAA J 51(1):94–106
5. Ong YS, Nair PB, Keane AJ (2003) Evolutionary optimization of computationally expensive problems via surrogate modeling. AIAA J 41(4):687–696
6. Yamamoto K, Inoue O (1995) Applications of genetic algorithm to aerodynamic shape optimization. Paper presented at the 12th computational fluid dynamics conference, San Diego, 19–22 June 1995
7. Matsushima K, Takanashi S, Iwamiya T (1997) Inverse design method for transonic multiple wing systems using integral equations. J Aircr 34(3):322–329
8. Hirose N, Takanashi S, Kawai N (1987) Transonic airfoil design procedure utilizing a Navier-Stokes analysis code. AIAA J 25(3):353–359
9. Obayashi S, Takanashi S (1996) Genetic optimization of target pressure distributions for inverse design methods. AIAA J 34(5):881–886
10. Takanashi S (1985) Iterative three-dimensional transonic wing design using integral equations. J Aircr 22(8):655–660
11. Koziel S, Pietrenko-Dabrowska A (2022) Low-cost quasi-global optimization of expensive electromagnetic simulation models by inverse surrogates and response features. Sci Rep 12(1):19894
12. Koziel S, Pietrenko-Dabrowska A (2022) Rapid design centering of multi-band antennas using knowledge-based inverse models and response features. Knowl-Based Syst 252:109360
13. Pietrenko-Dabrowska A, Koziel S (2021) Globalized parametric optimization of microwave components by means of response features and inverse metamodels. Sci Rep 11(1):23718
14. Koziel S, Pietrenko-Dabrowska A, Ullah U (2021) Low-cost modeling of microwave components by means of two-stage inverse/forward surrogates and domain confinement. IEEE Trans Microw Theory Tech 69(12):5189–5202
15. Pietrenko-Dabrowska A, Koziel S, Golunski L (2022) Two-stage variable-fidelity modeling of antennas with domain confinement. Sci Rep 12(1):17275
16. Koziel S, Pietrenko-Dabrowska A (2021) Global EM-driven optimization of multi-band antennas using knowledge-based inverse response-feature surrogates. Knowl-Based Syst 227:107189
17. Abdullah M, Koziel S (2021) A novel versatile decoupling structure and expedited inverse-model-based re-design procedure for compact single-and dual-band MIMO antennas. IEEE Access 9:37656–37667
18. Pietrenko-Dabrowska A, Koziel S, Ullah U (2022) Reduced-cost two-level surrogate antenna modeling using domain confinement and response features. Sci Rep 12(1):4667
19. Zhang YD, Huang JT, Gao ZH, Wang C, Shu BW (2019) Inverse design of low boom configurations using proper orthogonal decomposition and augmented Burgers equation. Chin J Aeronaut 32(6):1380–1389
20. Gu YR, Huang JT, Chen SS, Liu DY, Gao ZH (2023) Sonic boom inversion technology based on inverse augmented Burgers equation. Acta Aeronaut Astronaut Sin 44(2):626258 (in Chinese)
21. Aftosmis MJ, Nemec M, Cliff SE (2011) Adjoint-based low-boom design with Cart3D. Paper presented at the 29th AIAA applied aerodynamics conference, Honolulu, 27–30 June 2011
22. Nadarajah SK, Jameson A, Alonso JJ (2002) Sonic boom reduction using an adjoint method for wing-body configurations in supersonic flow. Paper presented at the 9th AIAA/ISSMO symposium on multidisciplinary analysis and optimization, Atlanta, 4–6 September 2002
23. Rallabhandi SK (2011) Sonic boom adjoint methodology and its applications. Paper presented at the 29th AIAA applied aerodynamics conference, Honolulu, 27–30 June 2011
24. Rallabhandi SK, Nielsen EJ, Diskin B (2014) Sonic-boom mitigation through aircraft design and adjoint methodology. J Aircr 51(2):502–510
25. Yang XR, Chen Y (2007) Atmospheric acoustics, 2nd edn. Science Press, Beijing (in Chinese)
26. Li W, Rallabhandi S (2014) Inverse design of low-boom supersonic concepts using reversed equivalent-area targets. J Aircr 51(1):29–36
27. Rallabhandi SK (2014) Application of adjoint methodology to supersonic aircraft design using reversed equivalent areas. J Aircr 51(6):1873–1882

28. Ma C, Huang JT, Liu G, Chen X, Shu BW, Chen QS et al (2023) Inversion technology of near-field sonic boom signal of supersonic aircraft. Acta Aerodyn Sin 41(4):1–10 (in Chinese)
29. Brunton SL, Nathan Kutz J, Manohar K, Aravkin AY, Morgansen K, Klemisch J et al (2021) Data-driven aerospace engineering: reframing the industry with machine learning. AIAA J 59(8):2820–2847
30. Glaws A, King RN, Vijayakumar G, Ananthan S (2022) Invertible neural networks for airfoil design. AIAA J 60(5):3035–3047
31. Sekar V, Zhang M, Shu C, Khoo BC (2019) Inverse design of airfoil using a deep convolutional neural network. AIAA J 57(3):993–1003
32. Wang C, Wang S, Wang L, Cao C, Sun G, Li C et al (2022) Framework of nacelle inverse design method based on improved generative adversarial networks. Aerosp Sci Technol 121:107365
33. Wang J, Li R, He C, Chen H, Cheng R, Zhai C et al (2022) An inverse design method for supercritical airfoil based on conditional generative models. Chin J Aeronaut 35(3):62–74
34. Ghosh S, Padmanabha GA, Peng C, Atkinson S, Andreoli V, Pandita P et al (2021) Pro-ML IDeAS: A probabilistic framework for explicit inverse design using invertible neural network. Paper presented at the AIAA Scitech 2021 forum, Virtual event, 11–15 & 19–21 January 2021
35. Cleveland RO (1995) Propagation of sonic booms through a real, stratified atmosphere. Dissertation, The University of Texas at Austin
36. Park MA, Carter MB (2021) Nearfield summary and analysis of the third AIAA sonic boom prediction workshop C608 low boom demonstrator. Paper presented at the AIAA Scitech 2021 Forum, Virtual event, 11–15 & 19–21 January 2021
37. Pang C, Gao ZH, Yang H, Chen SS (2021) An efficient grid assembling method in unsteady dynamic motion simulation using overset grid. Aerosp Sci Technol 110:106450
38. Chen SS, Cai FJ, Xiang XH, Gao ZH, Yan C (2021) A low-diffusion robust flux splitting scheme towards wide-ranging Mach number flows. Chin J Aeronaut 34(5):628–641
39. Chen SS, Gu YR, Yang H, Huang JT, Gao ZH (2022) Sonic boom prediction and uncertainly quantification analysis of a low-boom super-sonic aircraft. Acta Aerodyn Sin 41(4):1–11 (in Chinese)
40. Menter FR (1994) Two-equation eddy-viscosity turbulence models for engineering applications. AIAA J 32(8):1598–1605
41. Plotkin K, Sizov N, Morgenstern J (2008) Examination of sonic boom minimization experienced indoors. Paper presented at the 46th AIAA aerospace sciences meeting and exhibit, Nevada, 7–10 January 2008
42. Plotkin KJ (1989) Review of sonic boom theory. Paper presented at the 12th aeroacoustic conference, San Antonio, 10–12 April 1989

Publisher's Note